Variety of magnetic topological phases in the $(MnBi_2Te_4)(Bi_2Te_3)_m$ family

I. I. Klimovskikh,[1,*] M. M. Otrokov,[2,3,†] D. Estyunin,[1] S. V. Eremeev,[4,5,1] S. O. Filnov,[1] A. Koroleva,[1] E. Shevchenko,[1] V. Voroshnin,[6] I. P. Rusinov,[5,1] M. Blanco-Rey,[7,8] M. Hoffmann,[9] Z.S. Aliev,[10,11] M. B. Babanly,[12,13] I. R. Amiraslanov,[11,13] N.A. Abdullayev,[11] V.N. Zverev,[14] A. Kimura,[15] O.E. Tereshchenko,[16,17,1] K. A. Kokh,[18,17,1] L. Petaccia,[19] G. Di Santo,[19] A. Ernst,[9,20] P. M. Echenique,[8,7,2] N. T. Mamedov,[11] A. M. Shikin,[1] and E. V. Chulkov[2,7,8,1,‡]

[1] *Saint Petersburg State University, 198504 Saint Petersburg, Russia*
[2] *Centro de Física de Materiales (CFM-MPC), Centro Mixto CSIC-UPV/EHU, 20018 Donostia-San Sebastián, Basque Country, Spain*
[3] *IKERBASQUE, Basque Foundation for Science, 48011 Bilbao, Spain*
[4] *Institute of Strength Physics and Materials Science, Russian Academy of Sciences, 634055 Tomsk, Russia*
[5] *Tomsk State University, 634050 Tomsk, Russia*
[6] *Helmholtz-Zentrum Berlin für Materialien und Energie, Elektronenspeicherring BESSY II, Albert-Einstein-Strae 15, 12489 Berlin, Germany*
[7] *Departamento de Física de Materiales UPV/EHU, 20080 Donostia-San Sebastián, Basque Country, Spain*
[8] *Donostia International Physics Center (DIPC), 20018 Donostia-San Sebastián, Basque Country, Spain*
[9] *Institut für Theoretische Physik, Johannes Kepler Universität, A 4040 Linz, Austria*
[10] *Azerbaijan State Oil and Industry University, AZ1010 Baku, Azerbaijan*
[11] *Institute of Physics, National Academy of Sciences of Azerbaijan, AZ1143 Baku, Azerbaijan*
[12] *Institute of Catalysis and Inorganic Chemistry, Azerbaijan National Academy of Science, AZ1143 Baku, Azerbaijan*
[13] *Baku State University, AZ1148 Baku, Azerbaijan*
[14] *Institute of Solid State Physics RAS, Chernogolovka, Moscow district, Russia*
[15] *Department of Physical Sciences, Graduate School of Science, Hiroshima University, 1-3-1 Kagamiyama, Higashi-Hiroshima 739-8526, Japan*
[16] *A.V. Rzhanov Institute of Semiconductor Physics, Novosibirsk, 630090 Russia*
[17] *Novosibirsk State University, Novosibirsk, 630090 Russia*
[18] *V.S. Sobolev Institute of Geology and Mineralogy, Siberian Branch, Russian Academy of Sciences, Novosibirsk, 630090 Russian Federation*
[19] *Elettra Sincrotrone Trieste, Strada Statale 14 km 163.5, 34149 Trieste, Italy*
[20] *Max-Planck-Institut für Mikrostrukturphysik, Weinberg 2, D-06120 Halle, Germany*

(Dated: January 19, 2022)

Quantum states of matter combining non-trivial topology and magnetism attract a lot of attention nowadays; the special focus is on magnetic topological insulators (MTIs) featuring quantum anomalous Hall and axion insulator phases. Feasibility of many novel phenomena that *intrinsic* magnetic TIs may host depends crucially on our ability to engineer and efficiently tune their electronic and magnetic structures. Here, using angle- and spin-resolved photoemission spectroscopy along with *ab initio* calculations we report on a large family of intrinsic magnetic TIs in the homologous series of the van der Waals compounds $(MnBi_2Te_4)(Bi_2Te_3)_m$ with $m = 0, ..., 6$. Magnetic, electronic and, consequently, topological properties of these materials depend strongly on the m value and are thus highly tunable. The antiferromagnetic (AFM) coupling between the neighboring Mn layers strongly weakens on moving from MnBi2Te4 (m = 0) to MnBi4Te7 (m = 1), changes to ferromagnetic (FM) one in MnBi6Te10 (m = 2) and disappears with further increase in m. In this way, the AFM and FM TI states are respectively realized in the $m = 0, 1$ and $m = 2$ cases, while for $m \geq 3$ a novel and hitherto-unknown topologically-nontrivial phase arises, in which below the corresponding critical temperature the magnetizations of the non-interacting 2D ferromagnets, formed by the $MnBi_2Te_4$ building blocks, are disordered along the third direction. The variety of intrinsic magnetic TI phases in $(MnBi_2Te_4)(Bi_2Te_3)_m$ allows efficient engineering of functional van der Waals heterostructures for topological quantum computation, as well as antiferromagnetic and 2D spintronics.

I. INTRODUCTION

Magnetism and topology can meet each other both in real space, giving rise to complex magnetic structures such as vortices or skyrmions, and in reciprocal momentum space, resulting in Weyl semimetal or mag-

* ilya.klimovskikh@spbu.ru
† mikhail.otrokov@gmail.com
‡ evguenivladimirovich.tchoulkov@ehu.eus

netic topological insulator (MTI) phases. In the MTI case, the interplay between topology and magnetism provides particularly rich playground for realization of exotic physics. Below the magnetic critical temperature, the time-reversal symmetry breaks down introducing a mass term to the linear dispersion of Dirac fermions thus opening opportunities for realization of such phenomena as quantized anomalous Hall (QAH) and magnetoelectric effect, axion electrodynamics, or Majorana fermions.[1–5] These unusual properties make MTIs extremely attractive for applications in novel electronics and in the emerging 2D[6–8] and antiferromagnetic (AFM) spintronics.[9–11]

Until recently, the magnetism in TIs has been achieved using either magnetic doping[3,4,12–16], or proximity effect[17,18] as well as by construction of van der Waals (vdW) heterostructures[19–22]. This situation has changed drastically with the recent discovery of the AFM TI phase[23] in stoichiometric vdW layered antiferromagnet $MnBi_2Te_4$[24–28], which inspired a lot of research activity as it holds promise for realization of the high-temperature QAH and axion insulator states, Majorana hinge modes and other effects[23,25–27,29–33].

Here we propose the MTI family by introducing the $(MnBi_2Te_4)(Bi_2Te_3)_m$ series of vdW materials that, apart from $MnBi_2Te_4$ ($m = 0$), contains six more topologically-nontrivial compounds, namely $MnBi_4Te_7$ ($m = 1$), $MnBi_6Te_{10}$ ($m = 2$), $MnBi_8Te_{13}$ ($m = 3$), $MnBi_{10}Te_{16}$ ($m = 4$), $MnBi_{12}Te_{19}$ ($m = 5$) and $MnBi_{14}Te_{22}$ ($m = 6$). Along the series, the strength of the interlayer exchange interaction, that couples neighboring FM Mn layers, gradually decreases with the increase of m, while its character changes from an AFM ($m = 0, 1$) to FM ($m = 2$). It is then followed by a crossover into the purely 2D magnetic regime starting from $m = 3$. Combined with the non-trivial topology of the $(MnBi_2Te_4)(Bi_2Te_3)_m$ compounds, these magnetic states give rise to the AFM and FM TI phases for $m = 0, 1$ and $m = 2$, respectively, while for $m \geq 3$ a new MTI phase is formed in which, below the respective T_C, the magnetizations of the 2D FM-ordered Mn layers of the $MnBi_2Te_4$ building blocks are disordered along the [0001] directions. The topologically nontrivial nature of these compounds is confirmed by ARPES measurements that reveal the presence of the topological surface (TSS) states whose dispersion depends strongly on the crystal surface termination. The unusual magnetic properties make the $(MnBi_2Te_4)(Bi_2Te_3)_m$ series a unique tunable platform for creating various exotic states of matter such as intrinsic axion or QAH insulator[20,25,31], the field induced QAH insulator[30,31] or chiral topological superconductor.[32]

II. CRYSTAL STRUCTURE AND MAGNETIC CROSSOVER

The first compound in the $(MnBi_2Te_4)(Bi_2Te_3)_m$ series is $MnBi_2Te_4$ (m=0), which had been investigated previously and discovered to be the first AFM TI[24]. This system consists of septuple layer (SL) blocks stacked one on top of another. Each SL is a 2D ferromagnet, while the coupling between the neighboring SLs is antiferromagnetic.[24] For $m \geq 1$, the members of the $(MnBi_2Te_4)(Bi_2Te_3)_m$ family are comprised of alternating septuple ($MnBi_2Te_4$) and quintuple (Bi_2Te_3) layer blocks, see Fig.1a. The growth details and crystal structures of thus-formed $MnBi_4Te_7$ and $MnBi_6Te_{10}$ compounds have been first reported in Ref.34, for which the -5-7-5-7- and -5-5-7-5-5-7- blocks sequences corresponding to $m = 1$ and $m = 2$ have been respectively revealed.

The XRD patterns of our $MnBi_4Te_7$, $MnBi_6Te_{10}$, $MnBi_8Te_{13}$, $MnBi_{10}Te_{16}$, $MnBi_{12}Te_{19}$, and $MnBi_{14}Te_{22}$ samples, shown in Fig. S1 of Supplementary Information, confirm their $P\bar{3}m1$ and $R\bar{3}m$ space groups.

The temperature dependence of the resistivity measured in a zero magnetic field demonstrates the metallic-like behaviour for both $MnBi_4Te_7$ and $MnBi_6Te_{10}$, see Fig.1b,e. At low temperatures, the well-defined kinks at around $12 - 13$ K are observed for both compounds. As the external magnetic field is switched on and increased these features are washed out, pointing towards their magnetic origin. However, while thus-determined critical temperatures are almost the same for $MnBi_4Te_7$ and $MnBi_6Te_{10}$, the magnetic orders are different for these two compounds, as shown by means of SQUID magnetometry.

The field-cooled (FC) and zero-field cooled (ZFC) magnetic susceptibilities measured at 0.1 T for $MnBi_4Te_7$ are shown in Fig.1c. The high temperature paramagnetic behaviour ends up with a pronounced peak at 13 K, that is characteristic of an AFM ordering. The fitting of the susceptibility by the Curie-Weiss law yields the Curie-Weiss temperature (Θ_{CW}) of 13.2 K. Positive sign and relatively high value of Θ_{CW} (c.f. $3-6$ K for $MnBi_2Te_4$[24]) indicate the presence of strong ferromagnetic interactions in $MnBi_4Te_7$ in spite of the overall AFM behaviour. The Néel temperature of only 13 K for $MnBi_4Te_7$ versus 25 K for $MnBi_2Te_4$ reveals a strong weakening of the interlayer AFM coupling due to the insertion of the non-magnetic quintuple layer block (QL) between neighboring SLs. The onset of the ferromagnetic interactions is also manifested in splitting of the FC and ZFC curves at low temperature (spin-glass-like transition).

The $M(H)$ curves taken at various temperatures are presented in Fig.1d. Slightly below the Néel temperature (10 K) a typical AFM $M(H)$ behaviour takes place, with a spin-flip upturns appearing at 0.2 T, the latter value being much lower than that for $MnBi_2Te_4$ (3.5 T)[24]. At very low temperatures, the spin-flip hysteresis opens up in the magnetic field interval from 0.1 to 0.3 T, as seen for $T = 2$ K. Moreover, in the absence of external field, the magnetization does not fall to zero and forms a ferromagnetic hysteresis loop from -0.1 to 0.1 T. Such a dual complex metamagnetic behaviour can be explained by the presence of domains with ferro- and antiferromagnetic ordering between neighbor SLs. The presented data

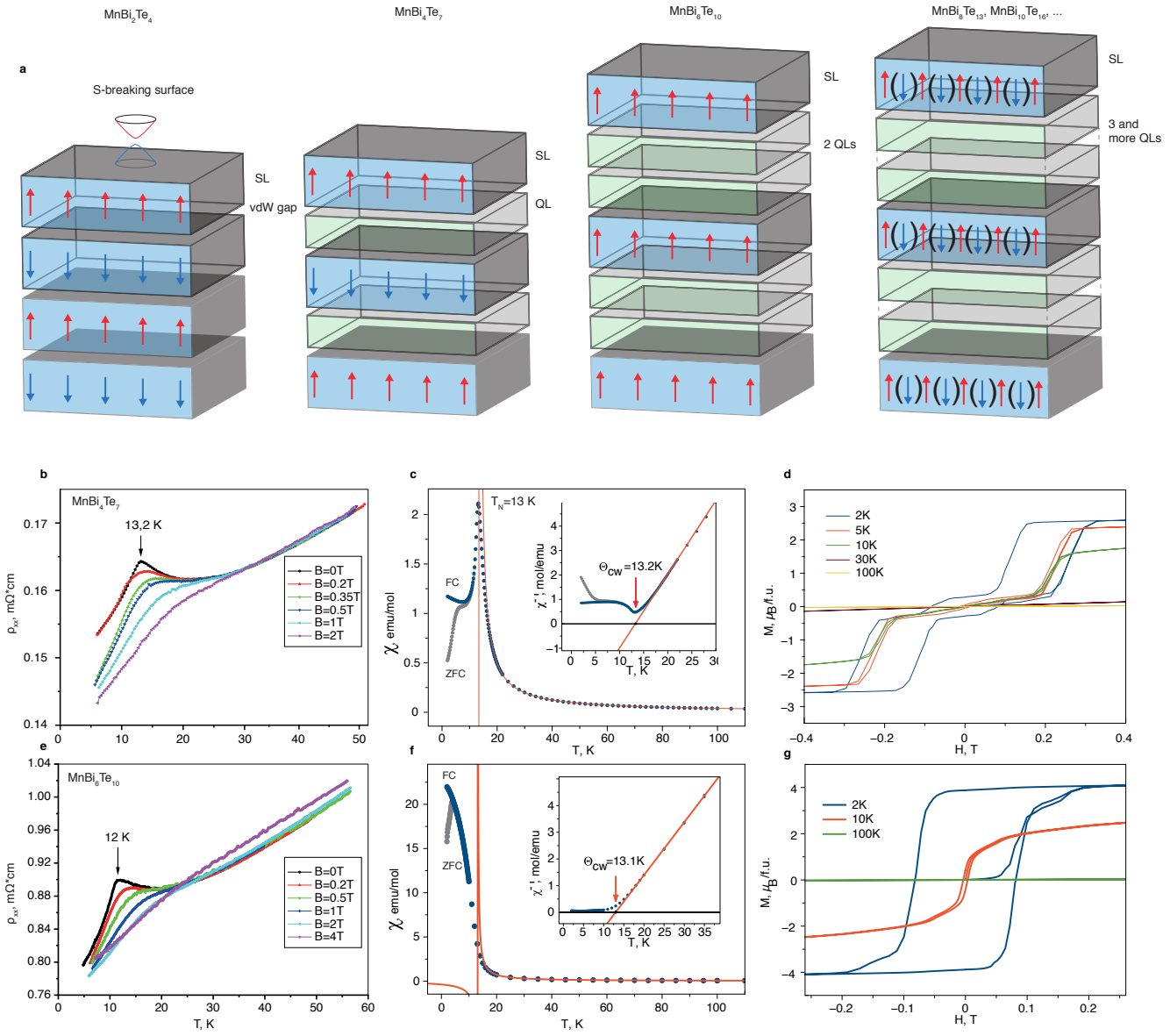

FIG. 1: **Magnetic structure of $(MnBi_2Te_4)(Bi_2Te_3)_m$ series.**
a Compounds $(MnBi_2Te_4)(Bi_2Te_3)_m$ consist of alternating five-layer (QL) and magnetic seven-layer (SL) blocks **b,e** Temperature dependence of the resistivity for $MnBi_4Te_7$ and $MnBi_6Te_{10}$ for various applied out-of-plane magnetic fields. **c,f** Magnetic susceptibility for $MnBi_4Te_7$ (c) and $MnBi_6Te_{10}$ (f) as a function of temperature measured in an external magnetic field of 0.1 T in zero-field-cooled and field-cooled conditions. Temperature-dependent reciprocal susceptibility is shown in the corresponding insets.The red line is a Curie-Weiss fit to the high-temperature data (see text for details). **d,g** Field dependent magnetization curves taken at various temperatures with out-of-plane external magnetic field for $MnBi_4Te_7$ (d) and $MnBi_6Te_{10}$ (g).

testify the weak 3D AFM/FM and strong 2D FM intralayer coupling in $MnBi_4Te_7$. Similar results with the metamagnetic behavior of $MnBi_4Te_7$ have been reported recently in Refs.35–38

The described experimental picture is consistent with that yielded by theory. Namely, the DFT exchange coupling parameters calculations reveal, first, a stable tendency to the intralayer FM ordering in the SLs of $MnBi_4Te_7$ and, second, a strong drop of the interlayer exchange coupling (1-2 orders of magnitude) as compared to $MnBi_2Te_4$ (see Supplementary Note II). Highly-accurate total-energy calculations give an energy difference between the FM and interlayer AFM configurations of 0.25 meV per Mn pair in favor of the interlayer AFM one. The magnetic anisotropy energy, E_a, is positive and equals to 0.12 meV (i.e. the easy axis is out-of-plane), which is roughly two times smaller than in bulk $MnBi_2Te_4$. In good agreement with the resistivity and

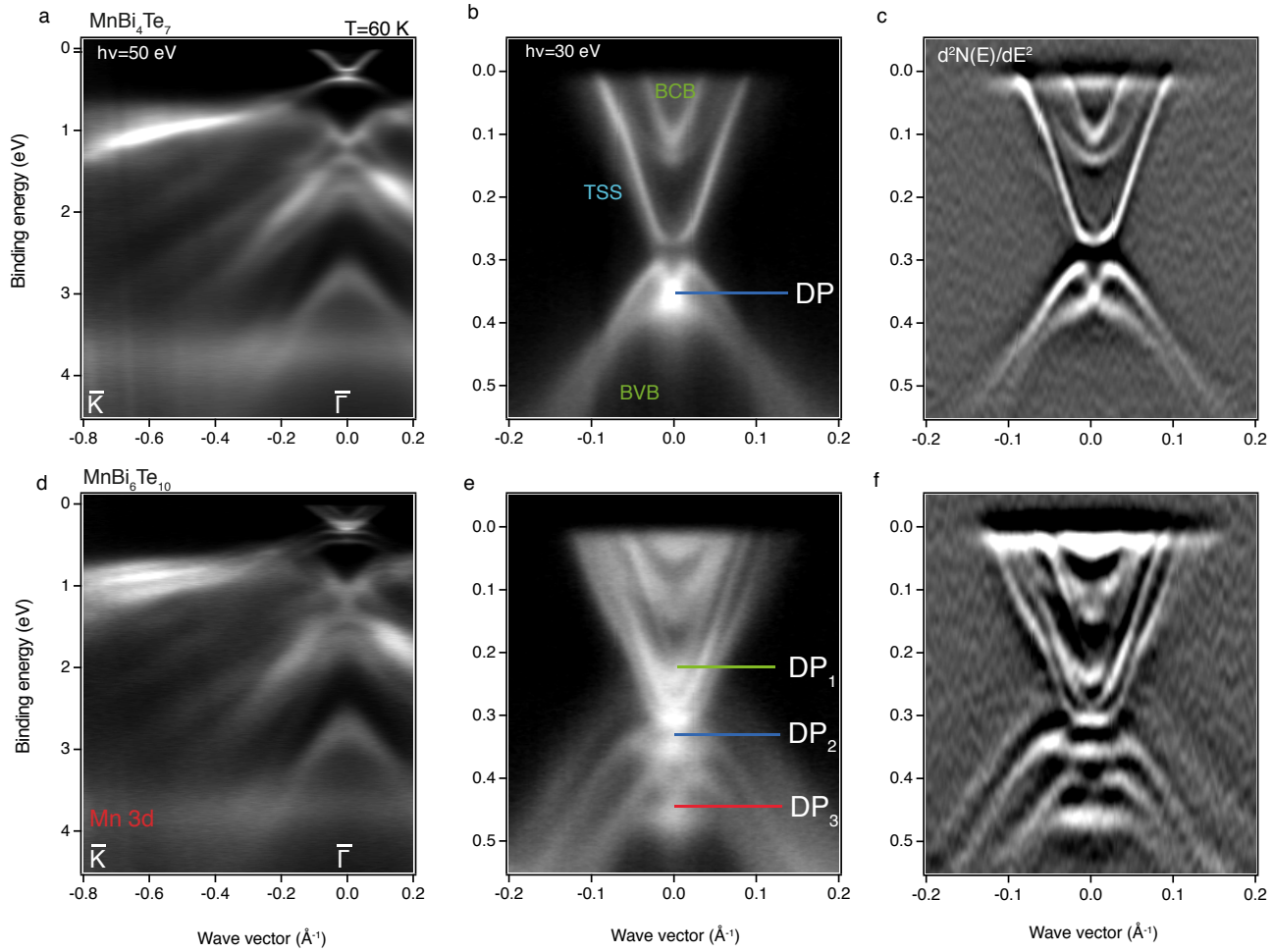

FIG. 2: **ARPES measurements of $MnBi_4Te_7$ and $MnBi_6Te_{10}$. a,d**, ARPES dispersion relations for the large energy and momentum region of $MnBi_4Te_7$ and $MnBi_6Te_{10}$ taken at 60 K at a photon energy of 50 eV; **b,e**, ARPES dispersion relations of the Dirac cone region taken at a photon energy of 30 eV at 60 K; **c,f** Second derivatives of the spectra presented in b,e.

magnetization measurements, our Monte Carlo simulations yield a Néel temperature of 13.6 K for the bulk $MnBi_4Te_7$. The drop of the Néel temperature from about 25 K in $MnBi_2Te_4$ to $\simeq$13 K in $MnBi_4Te_7$ is precisely caused by the weakening of the interlayer exchange coupling.

Increasing by one the number of QLs between SLs and forming $MnBi_6Te_{10}$ not only leads to further weakening of the interlayer exchange interaction, but also changes the character of the latter. The magnetic susceptibility data for this compound, shown in Fig.1f, do not exhibit any peak related to AFM ordering, while the FC and ZFC curves splitting and the Curie-Weiss fit ($\Theta_{CW} = 13.1$ K) reveal the same dominating intralayer ferromagnetic interactions as for $MnBi_4Te_7$. A pronounced hysteresis showing no spin-flip transitions is observed in the $M(H)$ curves, demonstrating an almost pure ferromagnetic behavior. Some deviations of the $M(H)$ curve slope at 0.05 T can be related to residual antiferromagnetic coupled domains. The DFT total-energy calculations performed for $MnBi_6Te_{10}$ show that the interlayer coupling weakens with respect to the $MnBi_4Te_7$ case, the difference between the AFM and FM states being 0.1 meV in favor of the AFM ordering. The discrepancy with the experimental results indicates that an overall FM behaviour may be caused by the n-doped character of the samples.

The $m = 3$ and 4 members of the series, i.e. $MnBi_8Te_{13}$ and $MnBi_{10}Te_{16}$, show an overall ferromagnetic behavior below the Curie temperatures of about 12 K, as revealed by the magnetization measurements (see Supplementary Fig. S4); a similar behaviour is expected for $MnBi_{12}Te_{19}$ ($m = 5$) and $MnBi_{14}Te_{22}$ ($m = 6$) because of the vanishing interlayer exchange interaction. In Ref. [25], the Curie temperature of the free-standing $MnBi_2Te_4$ SL has theoretically been predicted to be 12 K, which coincides with the values of $MnBi_8Te_{13}$ and $MnBi_{10}Te_{16}$. These facts allow us to conclude that the interlayer exchange coupling between SLs is practically absent in

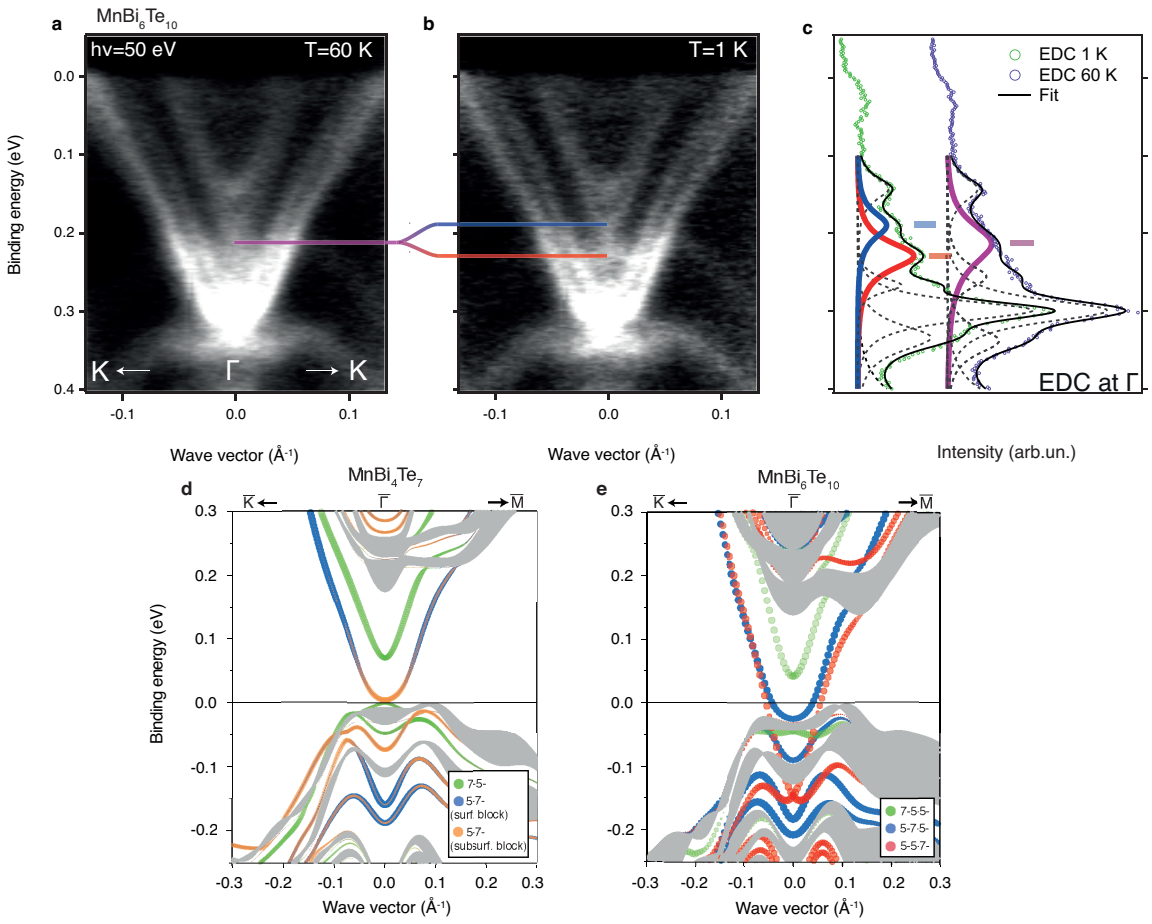

FIG. 3: **Temperature dependent ARPES measurements and DFT calculations a-c** ARPES measurements for $MnBi_6Te_{10}$ taken at 60 and 1 K, respectively and corresponding EDC profiles at $\overline{\Gamma}$-point with fitting results. The Dirac point gap opening can be seen as splitting of the magenta peak at 60 K to red and blue peaks at 1 K. **d**, Layer-resolved electronic structure of the $MnBi_4Te_7$ (0001) surface. The size of color circles reflects the weight of the state in the topmost block of the SL (green) and QL (blue) termination. The orange circles show the contribution of the subsurface (SL) block of the QL termination. The grey areas correspond to the bulk bandstructure projected onto the surface Brillouin zone. **e**, The same for $MnBi_6Te_{10}$ (0001) surface, the size of green, blue, and red circles reflects the weight of the state in the topmost block of the 7-5-5-, 5-7-5-, and 5-5-7- terminations.

$(MnBi_2Te_4)(Bi_2Te_3)_m$ with $m > 2$ and their magnetic structure can be described as a set of decoupled 2D ferromagnets whose magnetizations are randomly oriented – either parallel or antiparallel to the [0001] direction. Note that owing to the n-doping of the samples, the long-range RKKY exchange interaction may still weakly couple the magnetic layer blocks even for $m > 2$, although no indication of that has been observed in the experiment. Thus, the interlayer exchange interaction between the 2D FM SLs in the $(MnBi_2Te_4)(Bi_2Te_3)_m$ series first changes from AFM for $m = 0$ and 1 ($MnBi_2Te_4$ and $MnBi_4Te_7$) to FM for $m = 2$ ($MnBi_6Te_{10}$) and then practically disappears for $m \geq 3$ ($MnBi_8Te_{13}$, $MnBi_{10}Te_{16}$, $MnBi_{12}Te_{19}$ and $MnBi_{14}Te_{22}$). As we show next, these crossovers have profound consequences for the topological properties of the materials in this series.

III. TOPOLOGICAL SURFACE STATES

We now turn to the electronic structure study of the compounds in the $(MnBi_2Te_4)(Bi_2Te_3)_m$ series. As it has been mentioned above, the $MnBi_2Te_4$ ($m = 0$) compound was shown to be an AFM TI, its (0001) surface exhibiting the TSS with a gapped Dirac cone-like dispersion even above the T_N. The ARPES dispersion relations for the (0001) surface of the $MnBi_4Te_7$ compound ($m = 1$) measured at $T = 60$ K (low temperature measurements will be discussed below) are shown in Fig. 2a. Within the binding energy (BE) window from 0.5 to 4 eV, a quite complex bandstructure, characteristic of bismuth chalcogenides is seen[39,40]. However, unlike nonmagnetic TIs, a weakly dispersing state is discernible in Fig. 2a at the BE of about 3.8 eV, which is attributed to the Mn 3d-states, whose intensity is enhanced at the Mn-resonant photon

energy of 50 eV. Detailed ARPES dispersion relations in the low energy part of the spectrum are presented in Fig. 2b ($h\nu$ = 30 eV). Around the $\overline{\Gamma}$-point, there are two electron pockets that can be attributed to the bulk conduction bands of $MnBi_4Te_7$, clearly visible in the second derivative of the spectra, presented in Fig. 2c. Thus the material is n-doped which is typical of Bi-containing TIs[41]. The third electronic band, crossing the Fermi level, has largely a linear dispersion except for the close vicinity of the $\overline{\Gamma}$-point, where it becomes practically flat at the BE of 0.27 eV. At slightly higher BE, there is a M-shaped state, which is accompanied by a hole-like band with which it is degenerate at the Brillouin zone (BZ) center. Thus, between the linear and M-shaped bands a local gap is formed. Below the gap the electron-like part of the latter band behaves like a continuation of the linear band, as both have practically the same group velocity. To separate the bulk and surface states, ARPES measurements with various photon energies (50, 18 and 6 eV (laser)) have been performed, as presented in Supplementary Figure S6. The dispersion of the linear band does not show any photon energy dependence, which points towards its surface or 2D character. This allows to suggest that the linear band is the TSS, while far from the $\overline{\Gamma}$-poin the M-shaped band is likely to be the trivial surface state in the valence band that interacts with the TSS near the $\overline{\Gamma}$-point, leading to the appearance of the "avoided crossing" gap at the BE of 0.29 eV. In this case, the degeneracy point between the M-band and the close-lying hole band can be identified as the Dirac point (DP) of the $MnBi_4Te_7(0001)$ TSS. Since the TSS should be spin-polarized, spin-ARPES measurements have been performed. The acquired spectra (Supplementary Figure S6) clearly demonstrate the spin polarization reversal for opposite branches of the linear band, revealing the characteristic helical spin texture of the TSS. The performed bands assignment allows us to estimate the bulk band gap of $MnBi_4Te_7$ to be about 0.15 eV. It should be noted that on the surface of $MnBi_4Te_7$, since it is built of two different crystal blocks, QL and SL, two surface terminations and, consequently, two Dirac TSSs with different dispersion are expected in the ARPES spectrum. The absence of the second TSS will be discussed below.

The TSSs are also observed for the next member in $(MnBi_2Te_4)(Bi_2Te_3)_m$ series, $MnBi_6Te_{10}$ ($m = 2$). The ARPES dispersion relations for this compound are shown in Fig. 2d, measured at the same conditions as the spectrum in Fig. 2a. In the BE region from 1 to 5 eV, the valence band dispersions for $MnBi_6Te_{10}$ look similar to those of $MnBi_4Te_7$. Apparently, the intensity of the Mn-3d resonant feature seen at the BE of 3.8 eV is slightly decreased for $MnBi_6Te_{10}$, in accordance with the lower relative Mn concentration. The most pronounced difference between the band structures of the two compounds takes place in the region of BE between 1 eV and E_F, where the surface states dominate the photoemission signal. In particular, in Fig. 2d one can see three weakly dispersing states along the $\overline{\Gamma} - \overline{K}$ direction around the BE of 1 eV as well as three Dirac cones at the BZ center. This complex dispersion of the TSSs is resolved in the detailed ARPES image and its second derivative, shown in Fig.2e and f, where both the lower and upper parts of the three Dirac cones can be clearly seen.

The appearance of three TSSs at the $MnBi_6Te_{10}(0001)$ surface is caused by the peculiar crystal structure of the (m = 2) compound, built of the two types of blocks, stacked on top of each other in the -5-5-7-5-5-7- sequence. In such a case, the cleavage procedure leads to the formation of different surface terminations. Such a structure was previously observed for the $PbBi_6Te_{10}(0001)$ surface, where the three terraces were attributed to the 5-5-7-, 5-7-5- and 7-5-5- terminations, showing different dispersions of the TSS.[42] Similarly to $PbBi_6Te_{10}$, the cleaved surface of $MnBi_6Te_{10}$ may exhibit three types of terminations, two of them having a QL on the surface (i.e. either 5-5-7- or 5-7-5-), while the third possible crystal truncation is that by the SL (7-5-5-). Similarly to the $PbBi_6Te_{10}$ case, these terraces have different Dirac cone binding energies and spatial depth localization. The inner Dirac state (which by analogy with nonmagnetic TIs with similar structure can be assigned to the TSS generated by the SL-terminated terraces) shows the lowest BE ($\sim$0.25 eV) of the Dirac point (DP1) which is located above the bulk valence band states, while the other two cones (coming from different QL terraces) overlap with the bulk valence band (BVB).

The bulk phase transition from a paramagnetic to a ferromagnetic state is expected to affect the surface electronic structure. According to the DFT calculations shown in Fig. 3e, in the FM state the inner Dirac cone exhibits a giant mass gap of about 90 eV. To reveal such a behaviour in the experiment, we have measured ARPES spectra for $MnBi_6Te_{10}$ above and below the critical temperature, as shown in Fig. 3a,b. At 60 K, the DP of the SL termination TSS, located at a BE of 0.22 eV, consists of one broadened peak, as can be proved by energy distribution curves (EDCs) analysis presented in Fig. 3c. When the sample is cooled down to T = 1 K, the Dirac point splits by about 50 meV: the EDC fitting clearly shows the opening of the gap at the Dirac point. Note that this observation is possible because the DP of the SL termination (DP1 in Fig 2e) is well separated from the BVB, which is not the case for the QL terminations of $MnBi_6Te_{10}$. Strikingly, the DP exchange gap revealed for the SL-terminated $MnBi_6Te_{10}(0001)$ surface is closed in the paramagnetic phase, contrary to what happens in $MnBi_2Te_4$. The reason of this difference can lie in the reduced anisotropic spin fluctuations in comparison with $MnBi_2Te_4$[24], owing to the larger SL-SL distance and suppressed antiferromagnetic interaction. Finally, the electronic structure measurements performed for the $m = 3$ $MnBi_8Te_{13}(0001)$ and $m = 4$ $MnBi_{10}Te_{16}(0001)$ surfaces reveal the presence of the TSSs within the bulk band gap too (see Supplementary Information), but their analysis is complicated due to increased number of surface terraces after the cleavage.

According to the DFT electronic structure calculations, AFM bulk $MnBi_4Te_7$ features a fundamental band gap of 0.18 eV (Supplementary Note II). Because of its interlayer AFM ordering, $MnBi_4Te_7$ is invariant with respect to the combination of the time-reversal (Θ) and primitive-lattice translation ($T_{1/2}$) symmetries, $S = \Theta T_{1/2}$, and thus obeys the Z_2 topological classification of AFM insulators[23,43]. We find $Z_2 = 1$ for $MnBi_4Te_7$, meaning that its fundamental band gap is inverted whereby, similarly to $MnBi_2Te_4$, $MnBi_4Te_7$ is an AFM TI below the Néel temperature. The AFM TI state of $MnBi_4Te_7$ along with the out-of-plane direction of the staggered magnetization's easy axis dictate that there should be a gapped (gapless) TSS at the S-breaking (S-preserving) surface. This is exactly what we find: the TSS is gapped at both of the possible terminations of the $MnBi_4Te_7(0001)$ surface, which is S-breaking. At the SL termination, the DP gap is located inside the fundamental bulk band gap and reaches a large value of 70 meV. At the QL termination, a more complex surface electronic structure is revealed, with four bands located in the region of interest. To understand this spectrum, we have performed surface electronic structure calculations at different spin-orbit coupling (SOC) strengths. As it can be seen in Supplementary Fig. S9, with no SOC included there is an exchange-split trivial surface state in the valence bands' projected band gap around the $\overline{\Gamma}$-point at energy of about -0.3 eV. When the SOC is turned on and the system is in the topological phase, this spin-split state interacts with the TSS of the QL-termination, leading to the appearance of avoided crossings (Supplementary Fig. S9). At the natural SOC strength (Fig. 3d), these avoided crossing effects are quite significant and the Dirac cone appears to be torn in two parts, one of which is located in the fundamental band gap, while another in the projected band gap between approximately -0.1 and -0.2 eV. The split DP of the QL termination lies at about 0.16 eV below the Fermi level. The smaller DP gap size at the QL termination (about 29 meV) is caused by the predominant localization of the TSS in the surface block, whereby the interaction of this state with the Mn layer, lying in the subsurface block, is weaker. Thus, the complex dispersion of the QL-termination TSS is caused by the interaction with the trivial surface state, located in the bulk valence band. A comparison between the experimental and theoretical spectra allows identifying the measured surface bandstructure as that of the QL termination. In the PM state, the trivial surface state is exchange-unsplit which leads to a less complex appearance of the overall spectrum: there is only one avoided crossing clearly seen in ARPES in Fig. 2b. Thus, the gap in the TSS at a BE of about 0.27 eV (Fig. 2b) is indeed related to the "cut" of the Dirac cone by a trivial surface state and therefore this gap is observed above the Néel temperature. Cooling down below the magnetic critical point does not lead to significant changes (see Supplementary Figure S7), except for a slight broadening of the BVB, most likely related to the exchange splitting of the bulk states. Noteworthy, the SL–teminated Dirac cone is not seen in the ARPES spectra, the absence of its photoemission signal has also been reported for Pb- and Ge-based TIs in Refs. 44 and 45. Finally, our tight-binding calculations of the S-preserving $(10\bar{1}1)$ surface electronic structure reveal a gapless Dirac cone, as expected for an AFM TI (see Supplementary Figure S3).

The DFT-calculated (0001) surface band structure of the FM $MnBi_6Te_{10}$ is presented in Fig. 3e, where three Dirac cones are clearly seen in agreement with the ARPES data. Both the 7-5-5- and 5-7-5- terminations show essentially similar behaviors to those revealed for the $MnBi_4Te_7(0001)$. The TSS of the 5-5-7-termination is mostly located in the surface QL block and therefore its DP is almost unsplit.

Thus, all the compounds of the presented $(MnBi_2Te_4)(Bi_2Te_3)_m$ family are magnetic TIs, whose topological class changes with m. While $MnBi_2Te_4$ and $MnBi_4Te_7$ ($m = 0, 1$) are 3D AFM TIs, $MnBi_6Te_{10}$ ($m = 2$) turns out to be a 3D FM TI because of the change of the interlayer exchange coupling character. Starting from $m = 3$ the interlayer exchange interaction disappears, which has a very interesting consequence: $MnBi_8Te_{13}$, $MnBi_{10}Te_{16}$, $MnBi_{12}Te_{19}$, and $MnBi_{14}Te_{22}$ are the first examples of stoichiometric 3D MTI compounds in which the magnetizations of the 2D FM-ordered layers are disordered along the [0001] direction below the corresponding critical temperature.

The peculiar magnetic properties of the $(MnBi_2Te_4)(Bi_2Te_3)_m$ family combined with the nontrivial topology of its constituents enable observation of interesting effects for all of the presented members of the series. Those effects would take advantage of the interlayer exchange coupling tunability along the series, which is feasible through the changing of the number of QLs separating the SLs. This allows one to tailor both the strength and character of the interlayer exchange coupling and even to switch it off starting from $m \geq 3$. One particular consequence of it is that the magnetic structure, and therefore the topological class of the compounds can be tuned by an external magnetic field. This property is especially attractive in the 2D limit, where the $[MnBi_2Te_4]_{1SL}/(Bi_2Te_3)_{mQL(s)}/[MnBi_2Te_4]_{1SL}$ sandwiches, that can be obtained by careful exfoliation of the thin flakes from the single crystal surface,[30,31] turn to either the intrinsic zero plateau QAH state (also known as the axion insulator state) or the Chern insulator state. For $m \geq 3$, the latter state can be achieved in zero external magnetic field as has been earlier predicted by theory,[20] while for $MnBi_2Te_4$ and, probably, for $MnBi_4Te_7$ an external magnetic field is needed to achieve the quantized Hall effect.[30,31] However, in the $MnBi_4Te_7$ case, the strength of the critical field needed to overcome the AFM interlayer exchange coupling should be much smaller than that used for $MnBi_2Te_4$. The latter fact has also been pointed out as an advantage for a possible realization of the topological superconductor state based on the $(MnBi_2Te_4)(Bi_2Te_3)_m$ family, hosting

the exotic Majorana fermions[32]. From this point of view, the $(MnBi_2Te_4)(Bi_2Te_3)_m$ series represents a unique and highly tunable topological van-der-Waals platform for creation of both exotic topological phases and functional devices for antiferromagnetic and 2D spintronics as well as for topological quantum computing.

IV. CONCLUSIONS

In summary, we have reported the magnetic topological insulators family $(MnBi_2Te_4)(Bi_2Te_3)_m$ consisting of Mn-based magnetic septuple layer blocks separated by different number m of non-magnetic quintuple layers. The interlayer exchange coupling between the neighboring septuple layers can be tuned by changing m giving rise to a crossover from the interlayer antiferromagnetic ordering for $m = 0, 1$ ($MnBi_2Te_4$, $MnBi_4Te_7$) to the ferromagnetic one for $m = 2$ ($MnBi_6Te_{10}$) and, finally, to the complete disappearance of the interlayer interaction for $m \geq 3$ ($MnBi_8Te_{13}$, $MnBi_{10}Te_{16}$, $MnBi_{12}Te_{19}$ and $MnBi_{14}Te_{22}$). Combined with a non-trivial topology of the $(MnBi_2Te_4)(Bi_2Te_3)_m$ compounds, proven by ARPES, these magnetic states give rise to the AFM and FM TI phases for $m = 0, 1$ and $m = 2$, respectively, while for for $m \geq 3$ a new MTI phase is formed in which, below T_C, the magnetizations of the 2D FM-ordered Mn layers of the $MnBi_2Te_4$ building blocks are disordered along the [0001] direction. Depending on the surface terminations, a complex bundle of the Dirac cones is resolved by means of DFT and ARPES, and the magnetic gap in the Dirac point is found below the critical temperature. The tunable magnetic and topological phases in $(MnBi_2Te_4)(Bi_2Te_3)_m$ series allow engineering the promising platforms not only for QAH effect, axion insulators, and Majorana fermions, but also for emerging fields of antiferromagnetic and van-der-Waals 2D spintronics.

METHODS

Electronic structure and total-energy calculations

Electronic structure calculations were carried out within the density functional theory using the projector augmented-wave (PAW) method[46] as implemented in the VASP code[47,48]. The exchange-correlation energy was treated using the generalized gradient approximation[49]. The Hamiltonian contained scalar relativistic corrections and the SOC was taken into account by the second variation method[50]. In order to describe the van der Waals interactions we made use of the DFT-D2[51] and the DFT-D3[52,53] approaches, which gave similar results. The energy cutoff for the plane-wave expansion was set to 270 eV. All structural optimizations were performed using a conjugate-gradient algorithm and a force tolerance criterion for convergence of 0.01 eV/Å. Spin-orbit coupling was always included when performing relaxations. Depending on the particular task and geometry, different grids for the Brillouin zones (BZs) sampling were used (see below), all of them being $\overline{\Gamma}$-centered.

The Mn 3d-states were treated employing the GGA+U approach[54] within the Dudarev scheme[55]. The $U_{\text{eff}} = U - J$ value for the Mn 3d-states was chosen to be equal to 5.34 eV, as in previous works on $MnBi_2Te_4$ [19–21,24,25,56].

The bulk magnetic ordering was studied using total-energy calculations, performed for the FM and two different AFM states. Namely, we considered an interlayer AFM state and a noncollinear (NCL) intralayer AFM state, in which three spin sublattices form angles of 120° with respect to each other[56]. To model the FM and interlayer AFM structures in $MnBi_4Te_7$ and $MnBi_6Te_{10}$, we used cells with 24 and 34 atoms, respectively. For the $MnBi_4Te_7$ system, these calculations were performed with the respective 3D BZs sampled by the $25 \times 25 \times 5$ k-point grids. For the $MnBi_6Te_{10}$ compound, which exhibits extremely weak interlayer exchange coupling, the interlayer ordering was carefully studied using very fine k-meshes up to $23 \times 23 \times 19$ points. These meshes were also used in the magnetic anisotropy energy calculations. For $MnBi_4Te_7$, the noncollinear intralayer AFM configuration was treated using hexagonal bulk cell containing three atoms per layer [$(\sqrt{3} \times \sqrt{3})R30°$ in-plane periodicity] and a $11 \times 11 \times 3$ BZ sampling. For $MnBi_6Te_{10}$, NCL configuration has not been considered since all the available experimental and theoretical data in the literature indicate that each $MnBi_2Te_4$ SL block orders ferromagnetically, irrespectively of its structural environment.

The $MnBi_4Te_7$ and $MnBi_6Te_{10}$ semi-infinite surfaces were simulated within a model of repeating films separated by a vacuum gap of a minimum of 10 Å. The interlayer distances were optimized for the utmost SL or QL block of each surface. Both the structural optimizations and static electronic structure calculations were performed using a k-point grid of $11 \times 11 \times 1$ in the two-dimensional BZ.

The magnetic anisotropy energies, $E_a = E_{\text{diff}} + E_d$, were calculated taking into account both the total-energy differences of various magnetization directions $E_{\text{diff}} = E_{\text{in-plane}} - E_{\text{out-of-plane}}$, and the energy of the classical dipole-dipole interaction, E_d. To calculate E_{diff}, the energies for three inequivalent magnetization directions [cartesian x, y (in-plane) and z (out-of-plane)] were calculated and E_{diff} was determined as the difference $E_{\text{in-plane}} - E_z$, where $E_{\text{in-plane}}$ is the energy of the most energetically favorable in-plane direction of the magnetization. The total energies were calculated self-consistently for all considered directions. The energy convergence criterion was set to 10^{-7} eV providing a well-converged E_{diff} (up to a few tenth of meV) and excluding "accidental" convergence. A cutoff radius of at least 20 μm. was used to calculate E_d.

Exchange coupling constants calculations

For the equilibrium structure of $MnBi_4Te_7$ obtained with VASP, we calculated the Heisenberg exchange coupling constants $J_{0,i}$ also from first principles, within the full-potential linearized augmented plane waves (FLAPW) formalism[57] as implemented in FLEUR[58]. In the $J_{0,i}$ calculations SOC was neglected. We took the GGA+U approach[59,60] under the fully localised limit[61], using similar settings as those in Refs.24 and 25 The self-consistent FLAPW basis set Monkhorst-Pack k-point sampling of the first BZ and a cutoff of 3.4 Hartree. The cutoff energy for the density and potential expansions was 10.4 Hartree. Muffin tin sphere radii values of 2.74 a.u. for Mn and 2.81 a.u. for Bi and Te atoms were used, and the partial wave functions were expanded up to cutoffs of $l = 8$. Mn, Bi, and Te contribute $4s3d$, $5s5p$, and $6s6p$ valence electrons, respectively.

The $J_{0,i}$ constants were extracted by Fourier inversion of spin spirals in the reciprocal cell characterized by the q vectors of a $19 \times 19 \times 3$ grid. These dispersion energies, calculated in the force theorem approach, converged below 0.1 meV and allowed to add up to 150 neighbouring atoms to the Fourier analysis.

ARPES measurements

The experiments were carried out at 1-cubed UE-112 beamline at BESSY II in Berlin, BaDElPh beamline[62] at Elettra synchrotron in Trieste (Italy), BL-1, BL-9 and laser ARPES endstation at HiSOR in Hiroshima, and at Research Resource Center of Saint Petersburg State University "Physical methods of surface investigation" with a Scienta R4000 or a Specs Phoibos 150 energy analyzer. Samples were cleaved *insitu* at the base pressure of 6×10^{-11} mbar . The crystalline order and cleanliness of the surface were verified by low energy electron diffraction (LEED) and X-ray photoelectron spectroscopy (XPS).

Spin-resolved ARPES measurements were performed at BL-9 beamline of HiSOR synchrotron in Hiroshima and APE beamline at Elettra synchrotron in Trieste (Italy). The spectra were measured using VLEED spin detector. Total energy and angular resolutions were 20 meV and 1.5°, respectively.

SQUID magnetometry

Magnetic measurements were carried out in the resource center "Center for Diagnostics of Materials for Medicine, Pharmacology and Nanoelectronics" of the SPbU Science Park using a SQUID magnetometer with a helium cryostat manufactured by Quantum Design. The measurements were carried out in a pull mode in terms of temperature and magnetic field. The applied magnetic field was perpendicular to the (0001) sample surface.

Resistivity measurements

Resistivity measurements were done with a standard four-probe ac technique using a low-frequency (f∝20 Hz) Lock-in amplifier. Contacts were attached with conducting graphite paste. The measurements were carried out in a temperature-variable cryostat at different values of magnetic field up to 8 T, generated by a superconducting solenoid and directed along the normal to the (0001) sample surface.

ACKNOWLEDGMENTS

This work is supported by Saint Petersburg State University grant for scientific investigations (No. 15.61.202.2015) and Russian Science Foundation (grant No. 18-12-00062 in part of the photoemission measurements and 18-12-00169 in part of calculations of topological invariants, investigation of dependence the electronic spectra on SOC strength, and tight-binding band structure calculations). Russian Foundation for Basic Research (Grant No. 18-52-06009) and Science Development Foundation under the President of the Republic of Azerbaijan (Grant No. EIF-BGM-4-RFTF-1/2017-21/04/1-M-02) are acknowledged. We also acknowledge the support by the Basque Departamento de Educacion, UPV/EHU (Grant No. IT-756-13), Spanish Ministerio de Economia y Competitividad (MINECO Grant No. FIS2016-75862-P), and Tomsk State University competitiveness improvement programme (project No. 8.1.01.2017). The calculations were performed in Donostia International Physics Center and in the Research park of St. Petersburg State University Computing Center (http://cc.spbu.ru).

AUTHORS CONTRIBUTIONS

The manuscript has been written by I.I.K. and M.M.O. The ARPES measurements were carried out by I.I.K, A.M.S., D.E., V.V., S.O.F., G.S., L.P., A.Kimura. The SQUID magnetometry has been done by A.Koroleva. and E.S. The samples have been grown and characterized by Z.S.A., M.B.B., I.R.A, O.E.T. and K.A.K. The transport measurements have been carried out by N.Y.M., V.N.Z. and N.A.A. The band structure calculations were performed by M.M.O., S.V.E., I.P.R., M.B.R. The exchange coupling constants calculations were performed by M.B.R., M.M.O., and A.E. The magnetic anisotropy studies were performed by M.M.O. The Monte Carlo simulations were performed by M.H. The supervision of the project was executed by E.V.C. All authors contributed to the discussion and manuscript editing.

COMPETING FINANCIAL INTERESTS

Authors declare no competing financial interests.

[1] C.-X. Liu, X.-L. Qi, X. Dai, Z. Fang, and S.-C. Zhang, Phys. Rev. Lett. **101**, 146802 (2008).
[2] K. He, Y. Wang, and Q.-K. Xue, National Science Review **1**, 38 (2014).
[3] C.-Z. Chang, W. Zhao, D. Y. Kim, H. Zhang, B. A. Assaf, D. Heiman, S.-C. Zhang, C. Liu, M. H. Chan, and J. S. Moodera, Nat. Mat. **14**, 473 (2015).
[4] C.-Z. Chang, J. Zhang, X. Feng, J. Shen, Z. Zhang, M. Guo, K. Li, Y. Ou, P. Wei, L.-L. Wang, Z.-Q. Ji, Y. Feng, S. Ji, X. Chen, J. Jia, X. Dai, Z. Fang, S.-C. Zhang, K. He, Y. Wang, L. Lu, X.-C. Ma, and Q.-K. Xue, Science **340**, 167 (2013).
[5] Y. Feng, X. Feng, Y. Ou, J. Wang, C. Liu, L. Zhang, D. Zhao, G. Jiang, S.-C. Zhang, K. He, X. Ma, Q.-K. Xue, and Y. Wang, Phys. Rev. Lett. **115**, 126801 (2015).
[6] M. Gibertini, M. Koperski, A. F. Morpurgo, and K. S. Novoselov, Nature Nanotechnology **14**, 408 (2019).
[7] K. S. Burch, D. Mandrus, and J.-G. Park, Nature **563**, 47 (2018).
[8] X. Lin, W. Yang, K. L. Wang, and W. Zhao, Nature Electronics **2**, 274 (2019).
[9] T. Jungwirth, X. Marti, P. Wadley, and J. Wunderlich, Nat. Nanotech. **11**, 231 (2016).
[10] L. Šmejkal, Y. Mokrousov, B. Yan, and A. H. MacDonald, Nat. Phys. **14**, 242 (2018).
[11] V. Baltz, A. Manchon, M. Tsoi, T. Moriyama, T. Ono, and Y. Tserkovnyak, Rev. Mod. Phys. **90**, 015005 (2018).
[12] J. G. Checkelsky, J. Ye, Y. Onose, Y. Iwasa, and Y. Tokura, Nat. Phys. **8**, 729 (2012).
[13] Y. L. Chen, J. H. Chu, J. G. Analytis, Z. K. Liu, K. Igarashi, H. H. Kuo, X. L. Qi, S. K. Mo, R. G. Moore, D. H. Lu, M. Hashimoto, T. Sasagawa, S. C. Zhang, I. R. Fisher, Z. Hussain, and Z. X. Shen, Science **329**, 659 (2010).
[14] J. Henk, A. Ernst, S. V. Eremeev, E. V. Chulkov, I. V. Maznichenko, and I. Mertig, Phys. Rev. Lett. **108**, 206801 (2012).
[15] Y. S. Hor, P. Roushan, H. Beidenkopf, J. Seo, D. Qu, J. G. Checkelsky, L. A. Wray, D. Hsieh, Y. Xia, S.-Y. Xu, D. Qian, M. Z. Hasan, N. P. Ong, A. Yazdani, and R. J. Cava, Phys. Rev. B **81**, 195203 (2010).
[16] A. M. Shikin, A. A. Rybkina, D. A. Estyunin, D. M. Sostina, V. Y. Voroshnin, I. I. Klimovskikh, A. G. Rybkin, Y. A. Surnin, K. A. Kokh, O. E. Tereshchenko, L. Petaccia, G. Di Santo, P. N. Skirdkov, K. A. Zvezdin, A. K. Zvezdin, A. Kimura, E. V. Chulkov, and E. E. Krasovskii, Phys. Rev. B **97**, 245407 (2018).
[17] S. V. Eremeev, V. N. Men'shov, V. V. Tugushev, P. M. Echenique, and E. V. Chulkov, Phys. Rev. B **88**, 144430 (2013).
[18] F. Katmis, V. Lauter, F. S. Nogueira, B. A. Assaf, M. E. Jamer, P. Wei, B. Satpati, J. W. Freeland, I. Eremin, D. Heiman, P. Jarillo-Herrero, and J. S. Moodera, Nature **533**, 513 EP (2016).
[19] M. M. Otrokov, T. V. Menshchikova, I. P. Rusinov, M. G. Vergniory, V. M. Kuznetsov, and E. V. Chulkov, JETP Lett. **105**, 297 (2017).
[20] M. M. Otrokov, T. V. Menshchikova, M. G. Vergniory, I. P. Rusinov, A. Y. Vyazovskaya, Y. M. Koroteev, G. Bihlmayer, A. Ernst, P. M. Echenique, A. Arnau, and E. V. Chulkov, 2D Mater. **4**, 025082 (2017).
[21] T. Hirahara, S. V. Eremeev, T. Shirasawa, Y. Okuyama, T. Kubo, R. Nakanishi, R. Akiyama, A. Takayama, T. Hajiri, S. Ideta, *et al.*, Nano Lett. **17**, 3493 (2017).
[22] S. V. Eremeev, M. M. Otrokov, and E. V. Chulkov, *Nano Letters*, Nano Letters **18**, 6521 (2018).
[23] R. S. K. Mong, A. M. Essin, and J. E. Moore, Phys. Rev. B **81**, 245209 (2010).
[24] M. M. Otrokov, I. I. Klimovskikh, H. Bentmann, A. Zeugner, Z. S. Aliev, S. Gass, A. U. B. Wolter, A. V. Koroleva, D. Estyunin, A. M. Shikin, *et al.*, Preprint arXiv:1809.07389 (2018).
[25] M. M. Otrokov, I. P. Rusinov, M. Blanco-Rey, M. Hoffmann, A. Y. Vyazovskaya, S. V. Eremeev, A. Ernst, P. M. Echenique, A. Arnau, and E. V. Chulkov, Phys. Rev. Lett. **122**, 107202 (2019).
[26] D. Zhang, M. Shi, T. Zhu, D. Xing, H. Zhang, and J. Wang, Phys. Rev. Lett. **122**, 206401 (2019).
[27] J. Li, Y. Li, S. Du, Z. Wang, B.-L. Gu, S.-C. Zhang, K. He, W. Duan, and Y. Xu, Science Advances **5**, eaaw5685 (2019).
[28] Y. Gong, J. Guo, J. Li, K. Zhu, M. Liao, X. Liu, Q. Zhang, L. Gu, L. Tang, X. Feng, *et al.*, Chinese Physics Letters **36**, 076801 (2019).
[29] Y. Peng and Y. Xu, Phys. Rev. B **99**, 195431 (2019).
[30] Y. Deng, Y. Yu, M. Z. Shi, J. Wang, X. H. Chen, and Y. Zhang, arXiv preprint arXiv:1904.11468 (2019).
[31] C. Liu, Y. Wang, H. Li, Y. Wu, Y. Li, J. Li, K. He, Y. Xu, J. Zhang, and Y. Wang, arXiv preprint arXiv:1905.00715 (2019).
[32] J. Zhang, Z. Liu, and J. Wang, arXiv:1905.05919v1 (2019).
[33] J. Zhang, D. Wang, M. Shi, H. Zhang, and J. Wang, arXiv preprint arXiv:1906.07891 (2019).
[34] Z. S. Aliev, I. R. Amiraslanov, D. I. Nasonova, A. V. Shevelkov, N. A. Abdullayev, Z. A. Jahangirli, E. N. Orujlu, M. M. Otrokov, N. T. Mamedov, M. B. Babanly, and E. V. Chulkov, Journal of Alloys and Compounds **789**, 443 (2019).
[35] H. Sun, B. Xia, Z. Chen, Y. Zhang, P. Liu, Q. Yao, H. Tang, Y. Zhao, H. Xu, and Q. Liu, arXiv preprint arXiv:1905.12208 (2019).
[36] C. Hu, X. Zhou, P. Liu, J. Liu, P. Hao, E. Emmanouilidou, H. Sun, Y. Liu, H. Brawer, A. P. Ramirez, *et al.*, arXiv preprint arXiv:1905.02154 (2019).
[37] J. Wu, F. Liu, M. Sasase, K. Ienaga, Y. Obata, R. Yukawa, K. Horiba, H. Kumigashira, S. Okuma, T. Inoshita, *et al.*, arXiv preprint arXiv:1905.02385 (2019).
[38] R. C. Vidal, A. Zeugner, J. I. Facio, R. Ray, M. H. Haghighi, A. U. Wolter, L. T. C. Bohorquez, F. Caglieris, S. Moser, T. Figgemeier, *et al.*, arXiv preprint arXiv:1906.08394 (2019).

[39] A. M. Shikin, I. I. Klimovskikh, S. V. Eremeev, A. A. Rybkina, M. V. Rusinova, A. G. Rybkin, E. V. Zhizhin, J. Sánchez-Barriga, A. Varykhalov, I. P. Rusinov, E. V. Chulkov, K. A. Kokh, V. A. Golyashov, V. Kamyshlov, and O. E. Tereshchenko, Phys. Rev. B **89**, 125416 (2014).

[40] A. Bansil, H. Lin, and T. Das, Rev. Mod. Phys. **88**, 021004 (2016).

[41] M. Z. Hasan and C. L. Kane, Rev. Mod. Phys. **82**, 3045 (2010).

[42] M. Papagno, S. V. Eremeev, J. Fujii, Z. S. Aliev, M. B. Babanly, S. K. Mahatha, I. Vobornik, N. T. Mamedov, D. Pacilé, and E. V. Chulkov, ACS Nano **10**, 3518 (2016).

[43] C. Fang, M. J. Gilbert, and B. A. Bernevig, Phys. Rev. B **88**, 085406 (2013).

[44] S. V. Eremeev, G. Landolt, T. V. Menshchikova, B. Slomski, Y. M. Koroteev, Z. S. Aliev, M. B. Babanly, J. Henk, A. Ernst, L. Patthey, A. Eich, A. A. Khajetoorians, J. Hagemeister, O. Pietzsch, J. Wiebe, R. Wiesendanger, P. M. Echenique, S. S. Tsirkin, I. R. Amiraslanov, J. H. Dil, and E. V. Chulkov, Nature Communications **3**, 635 EP (2012).

[45] S. Muff, F. von Rohr, G. Landolt, B. Slomski, A. Schilling, R. J. Cava, J. Osterwalder, and J. H. Dil, Phys. Rev. B **88**, 035407 (2013).

[46] P. E. Blöchl, Phys. Rev. B **50**, 17953 (1994).

[47] G. Kresse and J. Furthmüller, Phys. Rev. B **54**, 11169 (1996).

[48] G. Kresse and D. Joubert, Phys. Rev. B **59**, 1758 (1999).

[49] J. P. Perdew, K. Burke, and M. Ernzerhof, Phys. Rev. Lett. **77**, 3865 (1996).

[50] D. D. Koelling and B. N. Harmon, J. Phys. C: Sol. St. Phys. **10**, 3107 (1977).

[51] S. Grimme, J. Comput. Chem. **27**, 1787 (2006).

[52] S. Grimme, J. Antony, S. Ehrlich, and H. Krieg, J. Chem. Phys. **132**, 154104 (2010).

[53] S. Grimme, S. Ehrlich, and L. Goerigk, J. Comput. Chem. **32**, 1456 (2011).

[54] V. I. Anisimov, J. Zaanen, and O. K. Andersen, Phys. Rev. B **44**, 943 (1991).

[55] S. L. Dudarev, G. A. Botton, S. Y. Savrasov, C. J. Humphreys, and A. P. Sutton, Phys. Rev. B **57**, 1505 (1998).

[56] S. V. Eremeev, M. M. Otrokov, and E. V. Chulkov, J. Alloys Compd. **709**, 172 (2017).

[57] E. Wimmer, H. Krakauer, M. Weinert, and A. J. Freeman, Phys. Rev. B **24**, 864 (1981).

[58] FLEUR site: http://www.flapw.de.

[59] V. I. Anisimov, F. Aryasetiawan, and A. I. Lichtenstein, Journal of Physics: Condensed Matter **9**, 767 (1997).

[60] A. B. Shick, A. I. Liechtenstein, and W. E. Pickett, Phys. Rev. B **60**, 10763 (1999).

[61] V. I. Anisimov, I. V. Solovyev, M. A. Korotin, M. T. Czyżyk, and G. A. Sawatzky, Phys. Rev. B **48**, 16929 (1993).

[62] L. Petaccia, P. Vilmercati, S. Gorovikov, M. Barnaba, A. Bianco, D. Cocco, C. Masciovecchio, and A. Goldoni, Nucl. Instrum. Methods Phys. Res. A **606**, 780 (2010).